13th International Conference on
Structural Health Monitoring of Intelligent Infrastructure
DOI: 10.3217/978-3-99161-057-1-121

Estimation of Wind Turbine Foundation Settlement and Error Modeling Using High-Resolution Dual-Orbit Satellite Data

Veronica Dallari[1, ORCID (0009-0005-0852-9763)], Elisa Bassoli[1, ORCID (0000-0002-4919-1421)], Francesca Grassi[1, ORCID (0000-0002-8493-0066)], Francesco Mancini[1, ORCID (0000-0002-8553-345X)], Loris Vincenzi[1, ORCID (0000-0003-2541-7104)]
[1]Department of Engineering Enzo Ferrari, University of Modena and Reggio Emilia, Via Pietro Vivarelli 10, 41125 Modena, Italy
email: veronica.dallari@unimore.it, elisa.bassoli@unimore.it, Francesca.grassi94@unimore.it, Francesco.mancini@unimore.it, loris.vincenzi@unimore.it

ABSTRACT: The demand for renewable energy sources is increasing, making it essential to develop effective maintenance plans for existing infrastructure. This study represents the initial step in a process designed to estimate the settlement of onshore wind turbine foundations, as well as its associated uncertainties. The method relies on high-resolution dual-orbit satellite data, which help to reduce cost and time required for instrument installation and on-site inspections. The turbine is modeled as a 1D rigid body and is assumed to be firmly constrained to the foundation slab. The proposed formulations allow for the estimation of the turbine motion components – translations in the W-E and vertical directions and rotation along the S-N axis –, which can be generally linked to foundation settlement. The components are determined by solving a linear system which accounts for the mean annual velocities of the Permanent Scatterers on the wind turbine surface, turbine height and incidence angles of satellite orbits. At the present stage, analytical formulations for the a posteriori estimation of the motion component uncertainties are proposed, with a particular focus on the positioning error in elevation of Permanent Scatterers. To assess the accuracy of these expressions, Monte Carlo numerical simulations are conducted. The strong agreement between numerical and analytical results demonstrates that the turbine motion components can be estimated with high accuracy.

KEY WORDS: Structural Health Monitoring; Foundation settlement; Wind turbines; Monte Carlo simulations; Uncertainty evaluation.

1 INTRODUCTION

As stated by the Global World Energy Council [1], the necessity to install new renewable energy sources grows stronger every year. In fact, to pursue the Paris Agreement goal – reducing greenhouse gas emissions by 43% by 2030 to limit global warming to 1.5°C – it was estimated that by 2030, 2 TW of wind energy will be installed. As for now, 78 GW of wind power capacity, of which 68.8 GW provided by onshore installations, were added globally in 2022.

In order to sustain the existing wind power structures, a solid maintenance plan is needed. Structural Health Monitoring (SHM) systems can contribute significantly to enhance wind turbines reliability and ensure their optimal performance, through different management approaches [2]. Various parts of the wind turbine, in fact, can be affected by structural issues, such as corrosion and cracks on the tower, or surface damage to the rotor blades [3]. Furthermore, particularly in the case of onshore installations, foundation settlement may occur: differential settlement, which manifests as tower rotation, can lead to a reduction in turbine efficiency, potentially resulting in economic losses. This phenomenon can take several months, or even years, to develop.

In [4], large vertical movements were observed in some onshore wind turbines, particularly in the case of concrete foundations in which embedded rings were used as connection systems, potentially leading to the sudden and catastrophic collapse of the turbine. Beyond the risk of structure failure, foundation settlement needs to be closely monitored for preserving the verticality of the tower and ensure an overall good health of the entire system. In particular, remote sensing techniques enable the investigation of foundation settlement while ensuring an off-site and non-invasive monitoring of the turbines.

Satellite data based monitoring was largely applied to investigate landslides and ground deformation in non-urban areas [5, 6], but, in the past few years, it also gained popularity in the structural field [7, 8]. In fact, multi-temporal Differential Interferometric Synthetic Aperture Radar (DInSAR) techniques allow obtaining the displacement information of several points, called Permanent Scatterers (PSs) [9], both on the ground and on reflective elements with millimetric precision [10] – also thanks to the developments of X band SAR systems [11].

Combining displacement information from both satellite orbits – ascending (ASC) and descending (DES) – of PSs belonging to structure surfaces, it is possible to obtain displacement information about the structure itself [12, 13]. For instance, through the use of high-resolution dual-orbit satellite data, it is possible to estimate the 3D rigid motion components of buildings, which can be generally linked to their foundation settlement [14]. Specifically, rigid translations can be an indicator of total settlement, while rigid rotations may indicate a differential settlement.

Besides the potential to investigate displacements over large areas with high accuracy, advantages of satellite data use in SHM include the possibility of portraying off-site and non-invasive monitoring, thus reducing both time and costs of instrument installation. Moreover, traditional monitoring equipment does not allow for obtaining results in a reasonable time if the foundation settlement phenomenon is slow; on the

DOI: 10.3217/978-3-99161-057-1-121

contrary, satellite techniques enable the analysis of past data - even 10 years before the time of analysis - proving to be effective when there is a need to obtain information from the past.

As part of a broader effort to detect potential foundation settlements in wind turbines, this paper introduces the initial stage of a procedure to estimate the 3D motion components of wind turbines using high-resolution dual-orbit satellite data. Formulations provided by Bassoli et al. [14] were adapted to the wind turbine case, which is modeled as a 1D rigid body. Also, analytical formulations for evaluating uncertainties regarding each motion component are presented. The main sources of error are related to measurement and positioning. Specifically, the measurement error includes the unavoidable uncertainties associated with measuring the displacements of PSs along the lines of sight. The positioning error refers to the uncertainties involved in placing the scatterers along the height of the turbine. At the present stage, a posteriori estimates of the uncertainties are presented and validated based on simulated data. Monte Carlo simulations were conducted to generate synthetic satellite data and obtain results under various conditions – detailed in section 3 – accounting for both primary sources of error. This allowed for a thorough assessment of the reliability of the proposed analytical expressions and supports their applicability to real-world scenarios. In future research, the procedure will be further developed by proposing a priori estimates based on simplified hypotheses and by applying them to real wind farms.

The paper is organized as follows. In section 777, analytical expressions relating 3D motion components of the turbine with displacement read along the line of sight are shown, as well as the procedure used to derive the uncertainties, with a specific emphasis on the positioning uncertainties. In section 3, the numerical simulations performed to verify the analytical expressions are outlined, while numerical and analytical results are presented and compared in section 4. Finally, conclusions are drawn.

2 IDENTIFICATION OF RIGID MOTION COMPONENTS FROM SATELLITE DATA

2.1 Geometry and satellite data definition

The wind turbine is modeled as a 1D rigid body firmly constrained to the foundation slab. Supposing that the slab-turbine connection happens at the exact center of gravity of the foundation, a reference system can be built as described: origin in the center of gravity (G), and *x*, *y* and *z* axes along the W-E, S-N and vertical directions respectively. In Figure 1, satellite geometry as well as an example of the PSs placement along the turbine height are reported. Note that all PSs are assumed to be aligned along the turbine *z*-axis; therefore, the planar positioning error is not considered.

In this study, all satellite geometry parameters — such as heading angles, measurement accuracy, and ground resolution — were assumed to match those of the COSMO-SkyMed constellation operating in StripMap mode over Italian regions. Specifically, the heading angles β_A and β_D, representing the satellite orbit inclination with respect to the S-N direction, were set to $\beta_A = 350°$ and $\beta_D = 190°$. The measurement accuracy was assumed to range from 1 to 2 mm/yr, and the ground resolution was taken as 3m×3m.

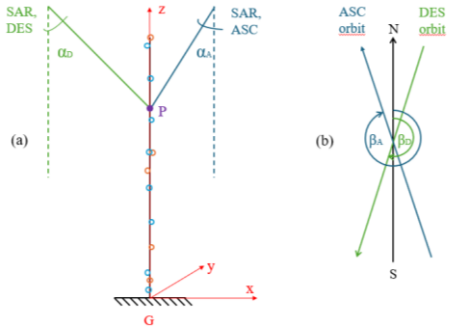

Figure 1. Satellite geometry: incidence angles and PSs positioning (a) and heading angles (b).

The same parameters were also used in the methodology to estimate rigid motion components and their associated uncertainties in [14]. The high resolution provided by this constellation makes COSMO-SkyMed data particularly well-suited for structural monitoring applications.

2.2 3D motion component estimation

In this study, the 3D rigid motion of wind turbines is estimated using the approach proposed by some of the authors in [14]. This method was originally developed to assess the motion of buildings modeled as 3D rigid bodies. Based on the structural geometry and satellite parameters, it allows for the evaluation of translations along the W-E and vertical directions, as well as rotations around the W-E, S-N, and vertical directions. The expressions proposed in [14] are adapted here to the case of wind turbines. Specifically, since the wind turbine is modeled as a 1D body, the rotation component along the *z*-axis was neglected. As with buildings, the translation along the S-N axis cannot be accurately assessed due to the limited sensitivity of SAR measurements in detecting displacements in the S-N direction [10, 15, 16].

It is important to emphasize that, to evaluate the full 3D rigid motion of the turbine, displacements of PSs measured in both orbits are required [15].

To avoid temporal misalignment of PSs displacements, the formulations are applied to the mean annual velocities of PSs (mm/yr), rather than to specific time instants. Additionally, due to the rigid motion assumption, spatial resampling to align PSs measured in ascending and descending orbits is unnecessary [17]: all permanent scatterers associated with the turbine contribute to the motion estimation.

Considering clockwise rotations as positive, the displacement of the generic point P with respect to G can be written as:

$$\begin{cases} v_{x,\mathrm{P}} = v_{x,\mathrm{G}} + \Phi_{y,\mathrm{G}} D_{z,\mathrm{P}} \\ v_{y,\mathrm{P}} = v_{y,\mathrm{G}} - \Phi_{x,\mathrm{G}} D_{z,\mathrm{P}} \\ v_{z,\mathrm{P}} = v_{z,\mathrm{G}} \end{cases} \quad (1)$$

where $v_{x,\mathrm{G}}$, $v_{y,\mathrm{G}}$, $v_{z,\mathrm{G}}$, represent the translations along the three directions while $\Phi_{x,\mathrm{G}}$ and $\Phi_{y,\mathrm{G}}$ are the rotations around the *x*- and *y*- axes. Finally, $D_{z,\mathrm{P}}$ indicates the elevation of point P relative to G.

The displacement of point P is then projected along the ascending and descending lines of sight (LOSs) of the satellite constellation. Incidence angles α_A and α_D indicate the inclination of the satellite LOSs with respect to the vertical

DOI: 10.3217/978-3-99161-057-1-121

direction, while β_A and β_D are the heading angles. Adopting the values reported in section 2.1, $\sin\beta_A$ and $\sin\beta_D$ can be approximated as 0 while $\cos\beta_A$ and $\cos\beta_D$ can be approximated as +1 and –1, respectively. Based on these considerations, and since that the translation component along the *y*-axis cannot be estimated due the limited sensitivity of SAR data in S-N direction, the displacement of point P projected onto the ascending and descending LOSs can be expressed as:

$$\begin{cases} d_{A,\mathrm{P}} = v_{z,\mathrm{G}}\cos\alpha_A - v_{x,\mathrm{G}}\sin\alpha_A - \Phi_{y,\mathrm{G}}D_{z,\mathrm{P}}\sin\alpha_A \\ d_{D,\mathrm{P}} = v_{z,\mathrm{G}}\cos\alpha_D + v_{x,\mathrm{G}}\sin\alpha_D + \Phi_{y,\mathrm{G}}D_{z,\mathrm{P}}\sin\alpha_D \end{cases} \quad (2)$$

A system of two equations in three unknowns – that are the translations in W-E and vertical directions and the rotation along the S-N direction – is obtained. To determine $v_{x,\mathrm{G}}$, $v_{z,\mathrm{G}}$ and $\Phi_{y,\mathrm{G}}$, at least three PSs from the two orbits are required. Assuming *n* PSs are available for the ascending orbit and *m* for the descending one, the system can be expressed as:

$$\begin{bmatrix} d_{A,1} \\ \vdots \\ d_{A,n} \\ d_{D,1} \\ \vdots \\ d_{D,m} \end{bmatrix} = \begin{bmatrix} -\sin\alpha_A & \cos\alpha_A & (-D_{z,1}\sin\alpha_A) \\ \vdots & \vdots & \vdots \\ -\sin\alpha_A & \cos\alpha_A & (-D_{z,n}\sin\alpha_A) \\ \sin\alpha_D & \cos\alpha_D & (D_{z,1}\sin\alpha_D) \\ \vdots & \vdots & \vdots \\ \sin\alpha_D & \cos\alpha_D & (D_{z,m}\sin\alpha_D) \end{bmatrix} \begin{bmatrix} v_{x,\mathrm{G}} \\ v_{z,\mathrm{G}} \\ \Phi_{y,\mathrm{G}} \end{bmatrix} \quad (3)$$

and can be synthesized as:

$$\mathbf{M} = \mathbf{S}\,\boldsymbol{\vartheta} \quad (4)$$

where $\mathbf{M}$ is a $Ns\times1$ vector, being $Ns=n+m$, containing PSs displacements along the LOSs, $\boldsymbol{\vartheta}$ is a 3×1 vector containing rigid motion components of the turbine, and $\mathbf{S}$ is a $Ns\times3$ matrix containing satellite geometries and the height of PSs.

Note that, due to measurement uncertainties thoroughly described in section 2.3, the theoretical displacement measurements in $\mathbf{M}$ are never exactly equal to the ones directly obtained from the satellite $\mathbf{M}^*$. Thus, to obtain the best $\boldsymbol{\vartheta}$ estimate, the least square operation must be applied:

$$\hat{\boldsymbol{\vartheta}} = (\mathbf{S}^{\mathrm{T}}\mathbf{S})^{-1}\,\mathbf{S}^{\mathrm{T}}\mathbf{M}^* \quad (5)$$

To assess the turbine motion relative to the ground, the terrain motion components must also be estimated and subtracted from the turbine motion. However, for the sake of simplicity, this study assumes the ground motion components to be zero.

2.3 Uncertainties estimation of rigid motion components

This section outlines the evaluation of the uncertainties associated to the above estimated motion components according to the procedure proposed in [14]. As previously stated, there are two main sources of error working with PS displacement data: measurement and positioning errors. Measurement error concerns the inevitable uncertainty committed when detecting the PS displacements along the LOSs, while positioning error regards the placement of the PS inside the resolution cell [14]. In this case, since PSs are supposed perfectly aligned to G, positioning uncertainties only regard the PS placement along the vertical direction. Using the product rule for derivatives, the variation of the $\boldsymbol{\vartheta}$ vector can be expressed as:

$$\Delta\boldsymbol{\vartheta} = \Delta\mathbf{B}\mathbf{M} + \mathbf{B}\Delta\mathbf{M} = \sum_{\mathrm{k}}\left(\frac{\partial\mathbf{B}}{\partial D_{z,k}}\right)\mathbf{M}\Delta D_{z,k} + \mathbf{B}\Delta\mathbf{M} \quad (6)$$

where $\mathbf{B} = (\mathbf{S}^{\mathrm{T}}\mathbf{S})^{-1}\mathbf{S}^{\mathrm{T}}$ represents the pseudo-inverse of matrix $\mathbf{S}$, $\mathbf{M}$ contains the PSs displacements along the LOSs, and $D_{z,k}$ is the elevation of the *k*-th PS. Lastly, $k=1,\ldots,n$ or $k=1,\ldots,m$ for the ascending or the descending PSs, respectively.

Assuming that measurement and positioning errors are not correlated [14], the total covariance matrix $\Sigma(\boldsymbol{\vartheta})$ can be expressed as the sum of the measurement covariance matrix and the positioning covariance matrix as follows:

$$\boldsymbol{\Sigma}(\boldsymbol{\vartheta}) = \boldsymbol{\Sigma}_{\mathbf{M}}(\boldsymbol{\vartheta}) + \boldsymbol{\Sigma}_{\mathbf{P}}(\boldsymbol{\vartheta}) \quad (7)$$

where the terms $\boldsymbol{\Sigma}_{\mathbf{M}}(\boldsymbol{\vartheta})$ and $\boldsymbol{\Sigma}_{\mathbf{P}}(\boldsymbol{\vartheta})$ indicate, respectively, contributions of measurement and positioning errors to the covariance matrix. Particularly, on the main diagonals, variances associated with each motion component can be found.

The covariance matrix associated to the measurement error $\boldsymbol{\Sigma}_{\mathbf{M}}(\boldsymbol{\vartheta})$ can be obtained as:

$$\boldsymbol{\Sigma}_{\mathbf{M}}(\boldsymbol{\vartheta}) = \mathbf{B}\,\boldsymbol{\Sigma}(\mathbf{M})\,\mathbf{B}^{\mathrm{T}} \quad (8)$$

Under the non-correlation hypothesis among the measures of PSs, $\boldsymbol{\Sigma}(\mathbf{M})$ can be assumed as a $Ns\times Ns$ diagonal matrix with terms equal to $\bar{\sigma}_{\mathrm{M}}^2$ on the main diagonal, representing the measurement accuracy. Thus, eq. (8) can be written as follows:

$$\begin{aligned}\boldsymbol{\Sigma}_{\mathbf{M}}(\boldsymbol{\vartheta}) = \bar{\sigma}_{\mathrm{M}}^2\mathbf{B}\mathbf{B}^{\mathrm{T}} = \bar{\sigma}_{\mathrm{M}}^2(\mathbf{S}^{\mathrm{T}}\mathbf{S})^{-1}\mathbf{S}^{\mathrm{T}}((\mathbf{S}^{\mathrm{T}}\mathbf{S})^{-1}\mathbf{S}^{\mathrm{T}})^{\mathrm{T}} = \\ = \bar{\sigma}_{\mathrm{M}}^2(\mathbf{S}^{\mathrm{T}}\mathbf{S})^{-1}\end{aligned} \quad (9)$$

According to section 2.1, typical values for $\bar{\sigma}_{\mathrm{M}}$ for COSMO-SkyMed data range from 1 to 2 mm/yr. However, to assess the applicability of the procedure, numerical simulations presented in the next section were conducted using values of 1, 2 and 5 mm/yr.

The positioning covariance matrix can be expressed as follows:

$$\boldsymbol{\Sigma}_{\mathbf{P}}(\boldsymbol{\vartheta}) = \left(\frac{\partial\mathbf{B}}{\partial\mathbf{D}}\mathbf{M}\right)\boldsymbol{\Sigma}(\mathbf{D})\left(\frac{\partial\mathbf{B}}{\partial\mathbf{D}}\mathbf{M}\right)^{\mathrm{T}} = \mathbf{J}\boldsymbol{\Sigma}(\mathbf{D})\mathbf{J}^{\mathrm{T}} \quad (10)$$

where $\mathbf{J}$ is the $3\times Ns$ Jacobian matrix whose components can be expressed as:

$$\mathbf{J}_k = \frac{\partial\boldsymbol{\vartheta}}{\partial D_{z,k}} = \begin{bmatrix} \frac{\partial v_{x,\mathrm{G}}}{\partial D_{z,k}} \\ \frac{\partial v_{z,\mathrm{G}}}{\partial D_{z,k}} \\ \frac{\partial \Phi_{y,\mathrm{G}}}{\partial D_{z,k}} \end{bmatrix} \quad (11)$$

$\mathbf{J}_k$ can also be written as:

$$\begin{aligned}\mathbf{J}_k = \frac{\partial\boldsymbol{\vartheta}}{\partial D_{z,k}} = \frac{\partial[(\mathbf{S}^{\mathrm{T}}\mathbf{S})^{-1}\mathbf{S}^{\mathrm{T}}]}{\partial D_{z,k}}\mathbf{M} = \\ \frac{1}{\left|(\mathbf{S}^{\mathrm{T}}\mathbf{S})\right|}\left[-\frac{\partial\left|(\mathbf{S}^{\mathrm{T}}\mathbf{S})\right|}{\partial D_{z,k}}\mathrm{I} + \frac{\partial\left[\mathrm{adj}(\mathbf{S}^{\mathrm{T}}\mathbf{S})\right]}{\partial D_{z,k}}\mathbf{S}^{\mathrm{T}}\mathbf{S} + \right. \\ \left. + \mathrm{adj}(\mathbf{S}^{\mathrm{T}}\mathbf{S})\frac{\partial\mathbf{S}^{\mathrm{T}}}{\partial D_{z,k}}\mathbf{S}\right]\boldsymbol{\vartheta}\end{aligned} \quad (12)$$

DOI: 10.3217/978-3-99161-057-1-121

with adj($\mathbf{S}^T\mathbf{S}$) and $|(\mathbf{S}^T\mathbf{S})|$ indicating the adjoint matrix and the determinant of $(\mathbf{S}^T\mathbf{S})$, respectively. Finally, $\mathbf{\Sigma}(\mathbf{D})$ is a diagonal matrix with elements $\overline{\sigma}_{Pz}^2$, representing the positioning accuracy along the vertical direction.

Monte Carlo simulations were carried out for estimating $\overline{\sigma}_{Pz}$, considering the resolution cell size of the COSMO-SkyMed constellation, equal to 3m×3m. The turbine tower can be divided into resolution segments *RS*s, which represent the projection of the ground resolution cell along the vertical direction. Random PS positions inside the ascending and descending resolution segments were simulated. The value of $\overline{\sigma}_{Pz}$ was defined as the standard deviation of the distance of the PS from the segment centre. For this specific case, the formulations were applied to incidence angles of $\alpha_A = 32.64°$ and $\alpha_D = 37.10°$. The obtained results are displayed in Table 1, while the trends of resolution segment lengths and standard deviations with the incidence angle are displayed in Figure 2. It is interesting to note that, since the resolution segment dimension depends on the incidence angles α_A and α_D, scatterers measured in the ascending orbit will display a different resolution than those measured in the descending orbit. In summary, the analytical formulation of the total uncertainty affecting each motion component can be derived by directly applying the error propagation law to both measurement and positioning errors:

$$\sigma_T(\vartheta_r) = \sqrt{\sigma_P^2(\vartheta_r) + \sigma_M^2(\vartheta_r)} \tag{13}$$

where $\sigma_M(\vartheta_r)$ and $\sigma_P(\vartheta_r)$ indicate, respectively, the measuring and positioning errors associated with the generic *r*-th motion component.

3 PROCEDURE FOR DATA SIMULATION

This section presents the numerical analyses designed to assess the performance of the procedure described in section 2. The analysis is based on: (i) applying rigid motion to an hypothetical turbine, (ii) simulating satellite measurements with incorporated measurement and positioning uncertainties, (iii) evaluating the rigid motion as outlined in section 2.2, (iv) comparing the imposed and estimated displacements, and (v) assessing the variability of the results.

The first step involved defining the geometric parameters of the wind turbine. A typical height of modern wind turbines is about 100 meters. For this reason, a maximum height *D* of 100 m was assumed. Next, the satellite characteristics of the COSMO-SkyMed constellation are chosen according to section 2.1. Incidence angles of the ascending and descending orbit are set equal to $\alpha_A = 32.64°$ and $\alpha_D = 37.10°$, respectively.

To simulate PS mean annual velocities and positions, motion component values needed to be imposed to the turbine, thus defining vector $\boldsymbol{\vartheta}$. Matrix **S** was reconstructed by incorporating

Table 1. Positioning accuracy.

Orbit	Incidence angle α [°]	Incidence angle α [rad]	Resolution segment *RS* [m]	Standard dev. $\overline{\sigma}_{Pz}$ [m]
ASC	32.64	0.57	4.684	1.351
DES	37.10	0.65	3.967	1.144

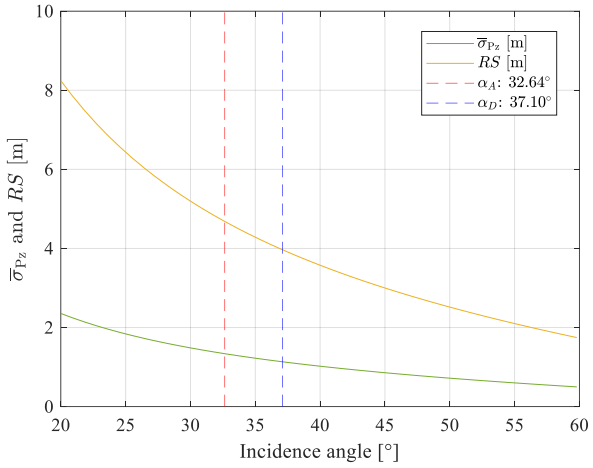

Figure 2. Trend of the standard deviation $\overline{\sigma}_{Pz}$ and of the resolution segment *RS* with the satellite incidence angle.

the previously defined satellite geometries and a specific number of PSs, which was constrained by an upper limit based on the tower height and the resolution cells dimensions.

To simulate the measurement errors, quantities extracted from a Gaussian distribution with zero mean and a standard deviation of $\overline{\sigma}_M$ were added to the velocities in vector **M**. Measurement uncertainties were assessed in the cases of $\overline{\sigma}_M$=1 mm/yr, $\overline{\sigma}_M$=2 mm/yr and $\overline{\sigma}_M$=5 mm/yr.

To clearly evaluate the impact of measurement and positioning errors, three scenarios are analyzed: the contribution of measurement errors alone, the contribution of positioning errors alone, and the effect of both. To account for the contribution of only measurement errors, the PSs were positioned at the exact center of each resolution segment. The PSs velocities along the lines of sight were then computed applying eq. (4). Instead, to account for only positioning errors, the PS velocities were kept without any uncertainties, while random errors were introduced into the PS heights within matrix **S**. These errors shifted the PSs positions randomly within their resolution segments, displacing them from the center but ensuring they remained within the segment boundaries. Finally, the case where both measurement and positioning uncertainties are considered was evaluated. Total uncertainty for each motion component was numerically estimated by combining the two approaches: both the PS velocities in vector **M** and the PS elevations in matrix **S** were perturbed from their exact values by adding random quantities extracted as described above. For quantifying the analytical uncertainty, the measurement and positioning errors formulas were combined through the error propagation law (eq. (13)).

For each of these three scenarios, the analytical error formulations were compared to the numerical ones across three different cases:

1) The PS number was kept constant, while the motion components were varied in discrete steps, ranging from zero to their maximum values according to Table 2.
2) The motion components were kept at a constant value – equal to the maximum one – while the PS number was varied from a minimum of two per orbit up to the maximum one;

DOI: 10.3217/978-3-99161-057-1-121

Table 2. Ranges of variation of the imposed motion parameters.

Motion component	Min value	Max value	Step
$v_{x,G}$ [mm/yr]	0	10	0.2
$v_{z,G}$ [mm/yr]	0	100	2
$\Phi_{y,G}$ [mrad/yr]	0	2	0.04

3) The PS number was kept constant, while one motion component at a time was varied in discrete steps, as in case 1), with the others held at a constant zero value.

For each step of the three cases, Monte Carlo simulations were performed to characterize the rigid motion component uncertainties, which are then compared with the analytical ones obtained from in eqs. (9), (10) and (13).

4 RESULTS

In this section, the results obtained for each of the cases outlined above will be discussed and presented in the form of graphs and tables. Note that, for simplicity, only the results related to the vertical translation and rotation of the turbine are shown, as they are considered the most representative of foundation settlement. However, the procedure can also be applied to W-E translation.

4.1 Measurement uncertainties

The first scenario, which includes only measurement errors and excludes positioning errors, is presented in this subsection. The results are presented in terms of the uncertainty values of the rigid motion components as the value of the component itself and the number of PSs on the structure vary.

4.1.1 Case 1: variation of the uncertainties with the motion amplitude

The results are presented in graph form (Figures 3 and 4) for the cases of $\bar{\sigma}_M$=1, 2 and 5 mm/yr. Both the error and the coefficient of variation (CoV) associated with each motion component are shown as the corresponding motion component varies. For clarity, results for the maximum step are also provided in Table 3 for the case of $\bar{\sigma}_M$= 2 mm/yr, which is considered the most representative measurement precision for this specific case.

As expected, both numerical and analytical uncertainties decrease as measurement accuracy increases – namely, the value of $\bar{\sigma}_M$ decreases. Additionally, it is important to note that the measurement uncertainty is independent on the motion component amplitude. This result is expected because eq. (8) states that the value of $\sigma_M(\vartheta)$ is independent on ϑ. On the other hand, the coefficient of variation of the uncertainty decreases if the motion component increases. As observed from both the tables and graphs, the numerical uncertainty appears to be well approximated by the analytical formulations at each motion step, indicating that the motion entity does not affect the accuracy of the analytical models.

4.1.2 Case 2: variation of the uncertainties with the number of PSs

The results are presented in Figures 5 and 6. The first graph depicts the values of $\sigma_M(v_{z,G})$ and the CoV of $v_{z,G}$ as a function of the number of PS in the ascending and descending orbits for the cases of $\bar{\sigma}_M$=1, 2 and 5 mm/yr, while the second one shows the values of $\sigma_M(\Phi_{y,G})$ and the CoV of $\Phi_{y,G}$ under the same conditions. For simplicity, the results are presented for the case where both orbits have the same number of PSs; in fact, the final step involves the use of 21 scatterers per orbit. Note that, as stated in section 2.2, n and m indicate, respectively, the number of PSs available for ascending and descending orbit.

Table 3. Measurement uncertainties on the rigid motion components - $\bar{\sigma}_M$=2 mm/yr, last step.

Component		$v_{x,G}$ [mm/yr]	$v_{z,G}$ [mm/yr]	$\Phi_{y,G}$ [mrad/yr]
Imposed		10.000	100.000	2.000
Simulated		9.992	100.002	2.000
$\sigma_M(\vartheta_r)$	Numerical	1.048	0.375	0.018
	Analytical	1.028	0.363	0.018
CoV(ϑ_r)	Numerical	10.48%	0.375%	0.917%
	Analytical	10.29%	0.363%	0.900%

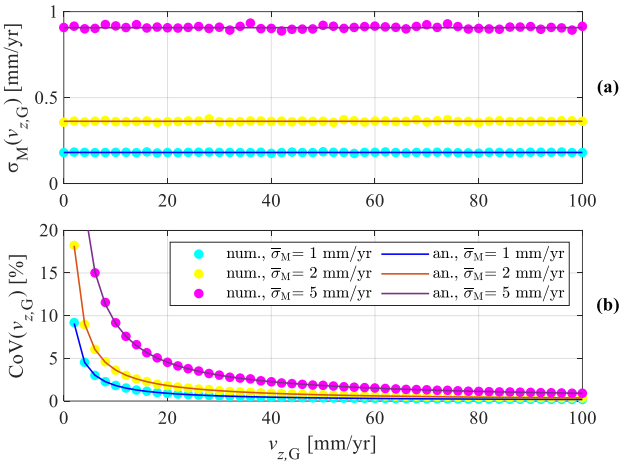

Figure 3. Influence of $v_{z,G}$ on the measurement uncertainties: (a) $\sigma_M(v_{z,G})$ and (b) CoV of $v_{z,G}$.

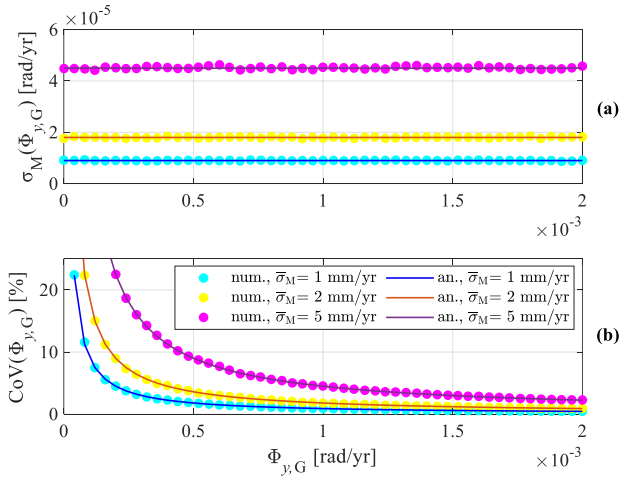

Figure 4. Influence of $\Phi_{y,G}$ on the measurement uncertainties: (a) $\sigma_M(\Phi_{y,G})$ and (b) CoV of $\Phi_{y,G}$.

DOI: 10.3217/978-3-99161-057-1-121

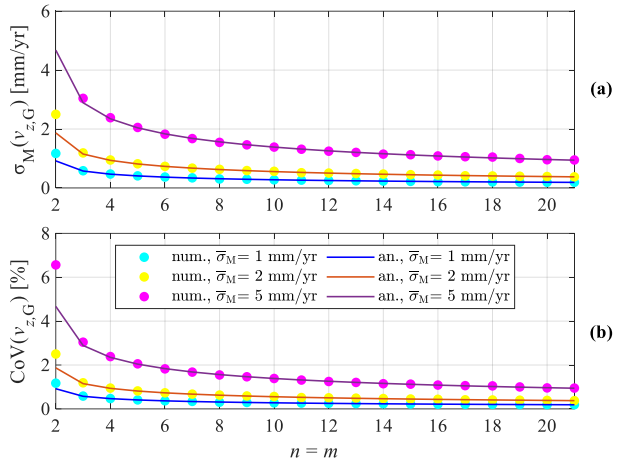

Figure 5. Influence of the PS number on the measurement uncertainties: (a) $\sigma_M(v_{z,G})$ and (b) CoV of $v_{z,G}$.

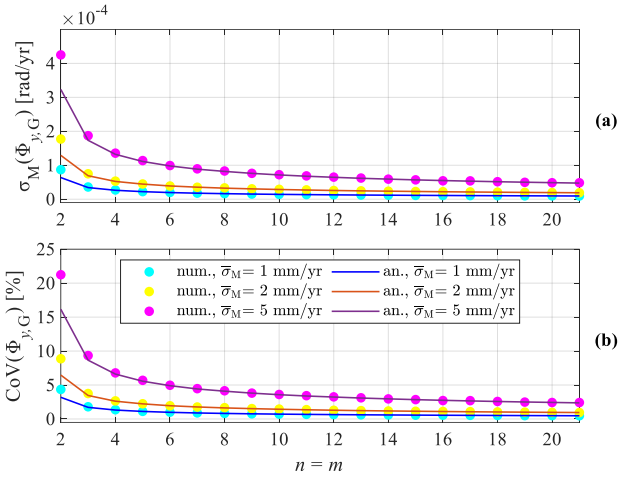

Figure 6. Influence of the PS number on the measurement uncertainties: (a) $\sigma_M(\Phi_{y,G})$ and (b) CoV of $\Phi_{y,G}$.

To obtain uncertainties, at least two permanent scatterers are required per orbit. The results corresponding to the maximum number of permanent scatterers align with those shown in Table 3 for the $\bar{\sigma}_M$= 2 mm/yr case. As expected, the uncertainties in the rigid motion parameters decrease as the number of PSs increases. For instance, in the case of S-N rotation $\Phi_{y,G}$, the coefficient of variation approaches nearly 20% if only 4 PSs are given and it decreases to a value less than 4% in the case of a number of PS greater than 18. Additionally, the numerical uncertainties appear to be well approximated by the analytical formulations, regardless of the PSs number. However, when only 2 scatterers per orbit are considered, the analytical formulations tend to underestimate the uncertainty, especially at lower measurement accuracy values. It can be observed that, to obtain significant results, at least five scatterers are needed in each orbit.

4.2 Positioning uncertainties

In this subsection, the results including only the positioning error are presented as a function of the amplitude of the motion component as well as of the number of observed PSs.

4.2.1 Case 1: variation of the uncertainties with the motion amplitude

Results are displayed in Figures 7, 8, and Table 4. The variation of $\sigma_P(v_{z,G})$ and CoV of $v_{z,G}$ with the value of $v_{z,G}$ are shown in Figure 7, while the variation of $\sigma_P(\Phi y_G)$ and CoV of Φy_G with the value of Φy_G are shown in Figure 8.

Numerical simulations were performed by introducing random perturbations to each PS position, as described in section 3. In contrast, analytical errors were computed using the method and parameters described in section 2.3.

The good agreement between the numerical and analytical uncertainties, as well as the CoVs for each motion component, demonstrates that the proposed analytical models provide a reliable approximation of the numerical errors, even in the case of positioning errors. It is also observed that, as predicted by eq. (12), positioning errors increase with the magnitude of the considered motion component, indicating that the positioning uncertainties do depend on the motion entity.

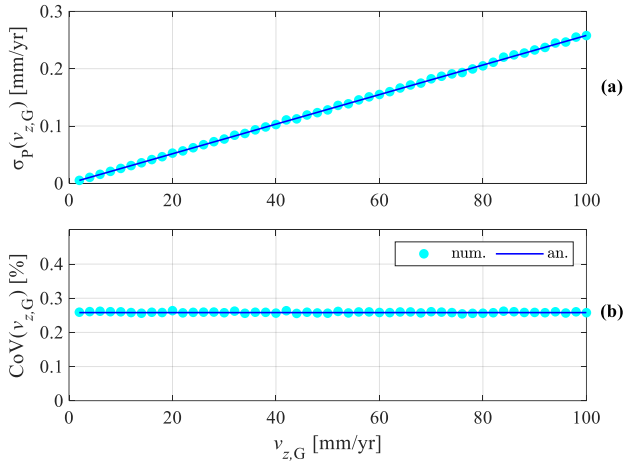

Figure 7. Influence of t $v_{z,G}$ on the positioning uncertainties: (a) $\sigma_P(v_{z,G})$ and (b) CoV of $v_{z,G}$.

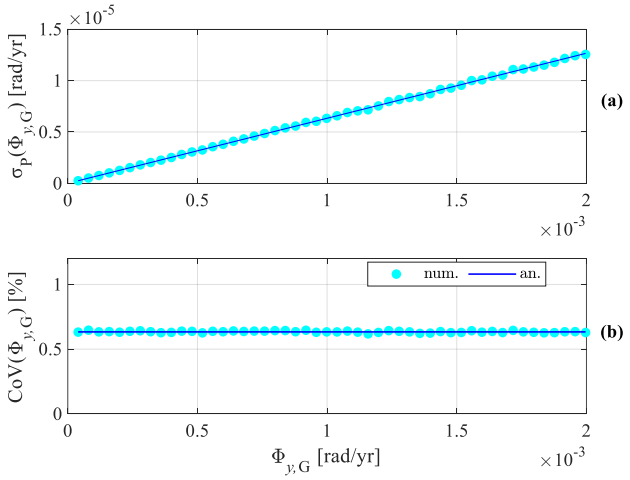

Figure 8. Influence of $\Phi_{y,G}$ on the positioning uncertainties: (a) $\sigma_P(\Phi_{y,G})$ and (b) CoV of $\Phi_{y,G}$.

DOI: 10.3217/978-3-99161-057-1-121

Table 4. Positioning uncertainties on the rigid motion components, last step.

Component		$v_{x,G}$ [mm/yr]	$v_{z,G}$ [mm/yr]	$\Phi_{y,G}$ [mrad/yr]
Imposed		10.000	100.000	2.000
Simulated		10.166	99.999	1.997
$\sigma_P(\vartheta_r)$	Numerical	0.718	0.259	0.013
	Analytical	0.723	0.258	0.013
$CoV(\vartheta_r)$	Numerical	7.06%	0.259%	0.634%
	Analytical	7.11%	0.258%	0.631%

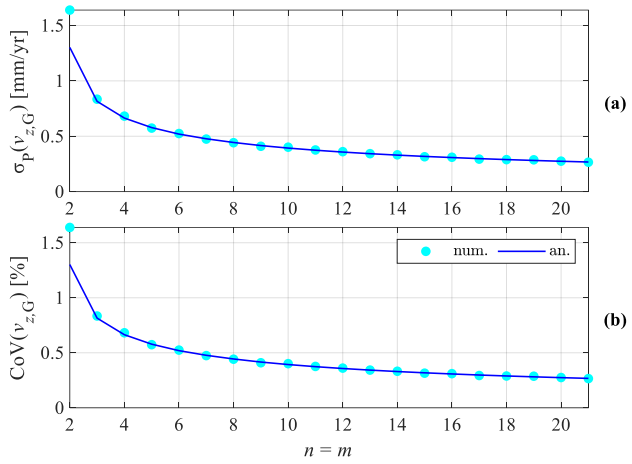

Figure 9. Influence of the PS number on the positioning uncertainties: (a) $\sigma_P(v_{z,G})$ and (b) CoV of $v_{z,G}$.

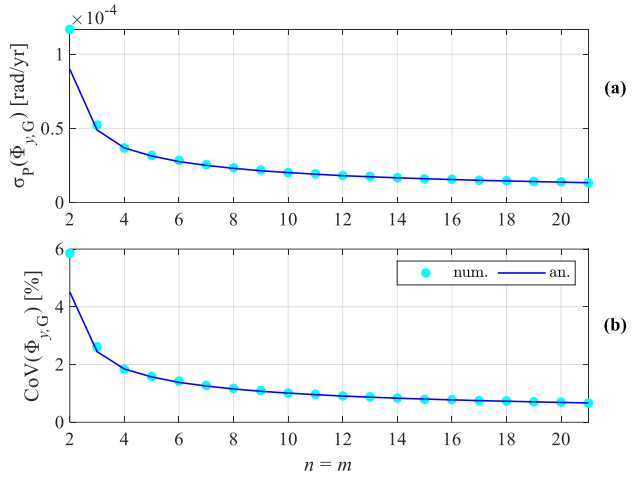

Figure 10. Influence of the PS number on the positioning uncertainties: (a) $\sigma_P(\Phi_{y,G})$ and (b) CoV of $\Phi_{y,G}$.

4.2.2 Case 2: variation of the uncertainties with the number of PSs

Figures 9 and 10 show the results as a function of the PS number. Specifically, Figure 9 illustrates the variation in positioning uncertainty $\sigma_P(v_{z,G})$ and in the CoV of $v_{z,G}$, while Figure 10 presents the variation in positioning uncertainty $\sigma_P(\Phi_{y,G})$ and in the coefficient of variation of $\Phi_{y,G}$.

Note that, in line with the measurement error case, the values of $\sigma_P(v_{z,G})$ and $\sigma_P(\Phi_{y,G})$ tend to increase as the number of PSs decreases. Specifically, although the numerical uncertainty is generally well approximated by the analytical formulations, when only 2 PSs per orbit are considered, the analytical formulations underestimate both the uncertainties and the coefficients of variation.

4.2.3 Case 1: variation of the uncertainties with the motion amplitude

As observed in the previous case, positioning error is indeed influenced by the motion entity. Therefore, it is crucial to identify which motion components have the greatest impact on the error. Figure 11, Figure 12 and Figure 13 show the variation in positioning uncertainty with the magnitude of the motion components. As shown, positioning errors seem to be uncorrelated with variations in $v_{x,G}$ and $v_{z,G}$. Specifically, their values are in the order of 10^{-10} mm/yr and rad/yr.

On the other hand, positioning errors appear to be strongly correlated with rotation; therefore, only the turbine's rotation can induce errors in the positioning of the PS.

Regardless of the variations in motion components, analytical formulations appear to provide a good approximation of numerical errors.

4.3 Total uncertainties

4.3.1 Case 1: variation of the uncertainties with the value of the motion component

Figures 14 and 15 display the results in the form of graphs: as previously stated, the considered positioning precision is detailed in

, while for immediacy measurement precision is fixed at $\bar{\sigma}_M$= 2 mm/yr. Particularly, Figure 14 details how the variation in $v_{z,G}$ influences the total error $\sigma_T(v_{z,G})$ and CoV of $v_{z,G}$, while Figure 15 illustrates the total error $\sigma_T(\Phi_{y,G})$ and CoV of $\Phi_{y,G}$ as a function of $\Phi_{y,G}$. For the sake of clarity, results regarding the maximum $v_{z,G}$ and $\Phi_{y,G}$ values are also displayed in table form in Table 5.

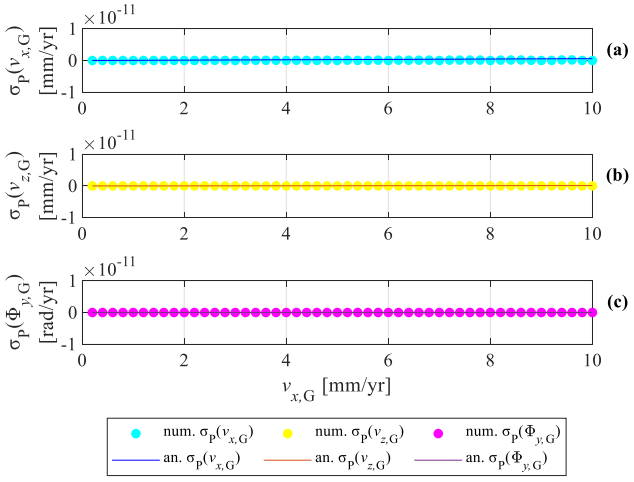

Figure 11. Influence of $v_{x,G}$ on the positioning uncertainties: σ_P of $v_{x,G}$ (a), $v_{z,G}$ (b) and $\Phi_{y,G}$ (c).

DOI: 10.3217/978-3-99161-057-1-121

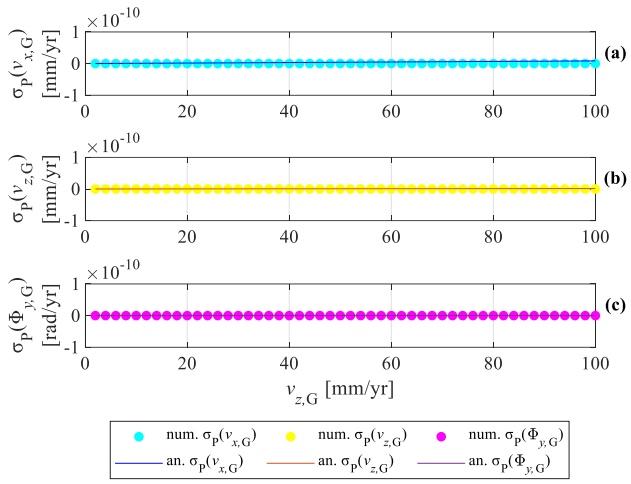

Figure 12. Influence of $v_{z,G}$ on the positioning uncertainties: σ_P of $v_{x,G}$ (a), $v_{z,G}$ (b) and $\Phi_{y,G}$ (c).

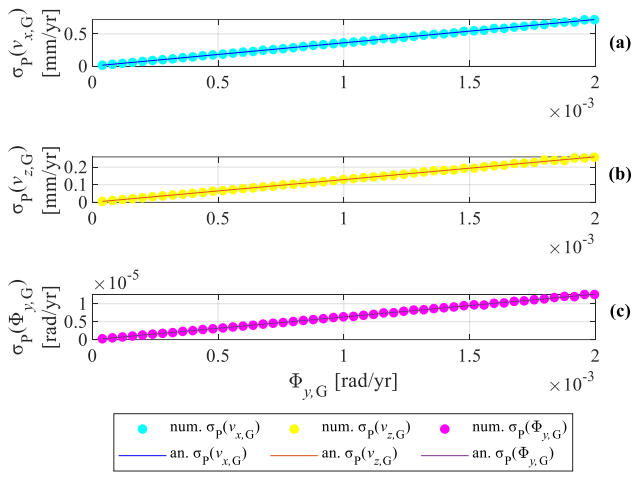

Figure 13. Influence of $\Phi_{y,G}$ on the positioning uncertainties: σ_P of $v_{x,G}$ (a), $v_{z,G}$ (b) and $\Phi_{y,G}$ (c).

Numerical simulations of uncertainties were performed as outlined in section 3. In contrast, analytical errors were computed using the method and parameters described in Section 2.3; in particular, adopting the formula described in equation (13). The good agreement between the numerical and analytical uncertainties, as well as the CoVs for each motion component, demonstrates that the proposed analytical models provide a reliable approximation of the numerical errors, even in the case of total errors. Note that measurement errors seem to be the largest contributor to the total uncertainty, while positioning error becomes a more significant factor as the motion component increases.

4.3.2 Case 2: variation of the uncertainties with the number of PSs

In Figure 16, the variations of the total error $\sigma_T(v_{z,G})$ and of the total CoV of $v_{z,G}$ as a function of PSs number are displayed. Moreover, Figure 17 depicts the variation of the total error $\sigma_T(v_{z,G})$ and of the total CoV of $v_{z,G}$ as a function of PSs number. Note that, as anticipated, errors increase as the number of PSs decreases.

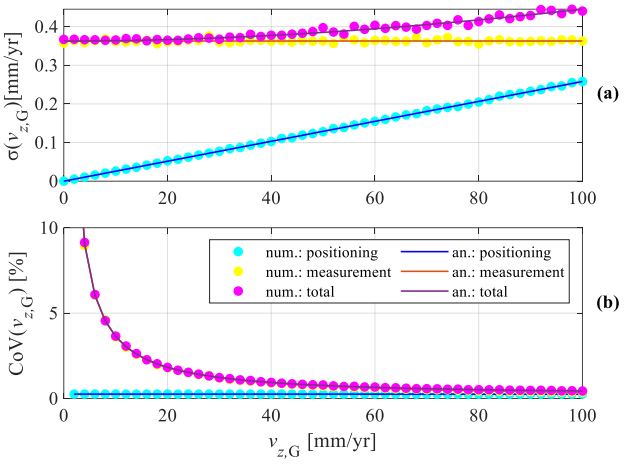

Figure 14. Influence of $v_{z,G}$ on the total uncertainties: (a) $\sigma(v_{z,G})$ and (b) CoV of $v_{z,G}$.

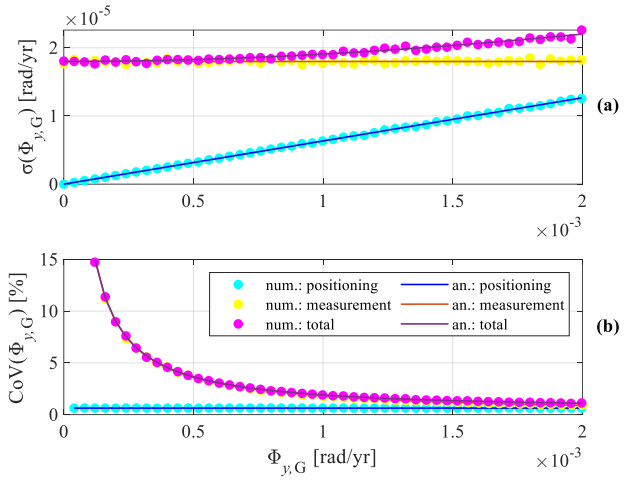

Figure 15. Influence of $\Phi_{y,G}$ on the total uncertainties: (a) $\sigma(\Phi_{y,G})$ and (b)CoV of $\Phi_{y,G}$.

Table 5. Total uncertainties on the rigid motion components - $\bar{\sigma}_M$=2 mm/yr, last step.

Component		vx_G [mm/yr]	vz_G [mm/yr]	Φy_G [mrad/yr]
Imposed		10.000	100.000	2.000
Simulated		10.143	99.996	1.997
$\sigma_T(\vartheta_r)$	Numerical	1.273	0.447	0.022
	Analytical	1.248	0.444	0.022
$CoV(\vartheta_r)$	Numerical	12.55%	0.447%	1.119%
	Analytical	12.31%	0.444%	1.092%

Similarly to the cases of measurement and positioning uncertainties, the numerical uncertainty is generally well approximated by the analytical formulations. The only exception occurs when 2 scatterers per orbit are considered, where the analytical formulations underestimate the numerical errors.

DOI: 10.3217/978-3-99161-057-1-121

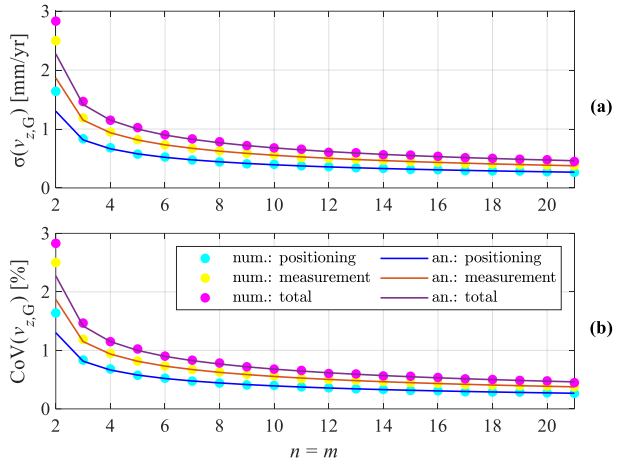

Figure 16. Influence of the PS number on the total uncertainties: (a) $\sigma(v_{z,G})$ and (b) CoV of $v_{z,G}$.

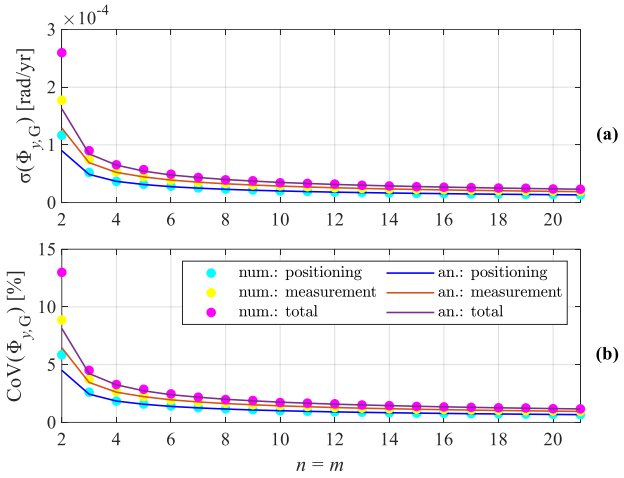

Figure 17. Influence of the PS number on the total uncertainties: (a) $\sigma(\Phi_{y,G})$ and (b) CoV of $\Phi_{y,G}$.

4.3.3 Case 1: variation of the uncertainties with the motion amplitude

Results are presented in Figures 18, 19 and 20. In particular, the three graphs depict how the variations in $v_{x,G}$, $v_{z,G}$ and $\Phi_{y,G}$, respectively, influence the total errors $\sigma_T(v_{x,G})$, $\sigma_T(v_{z,G})$ and $\sigma_T(\Phi_{y,G})$.

As already observed in the positioning uncertainties case, the rotation appears to be the only motion component affecting the uncertainty, while the translations have no effect on the error. Specifically, an increase in $\Phi_{y,G}$ directly translates in an increase of the component total errors. In any case, the analytical formulations provide an effective approximation of the numerical errors: their quality is validated by their accurate approximation of numerical errors in each of the presented cases.

CONCLUSIONS

This paper proposes a method for estimating the 3D rigid motion components of wind turbines and the corresponding uncertainties using DInSAR satellite data.

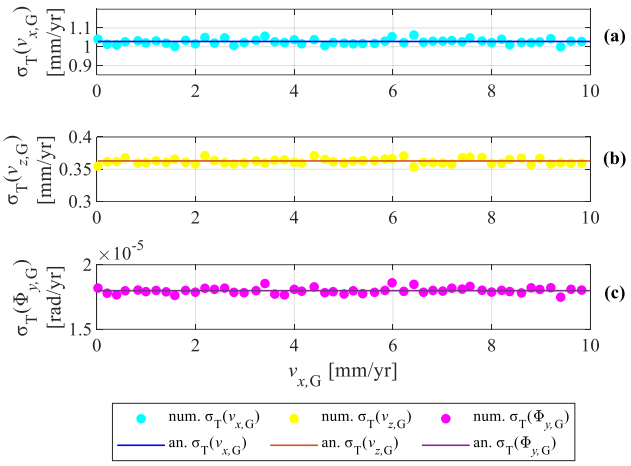

Figure 18. Influence of $v_{x,G}$ on the total uncertainties: σ_T of $v_{x,G}$ (a), $v_{z,G}$ (b) and $\Phi_{y,G}$ (c).

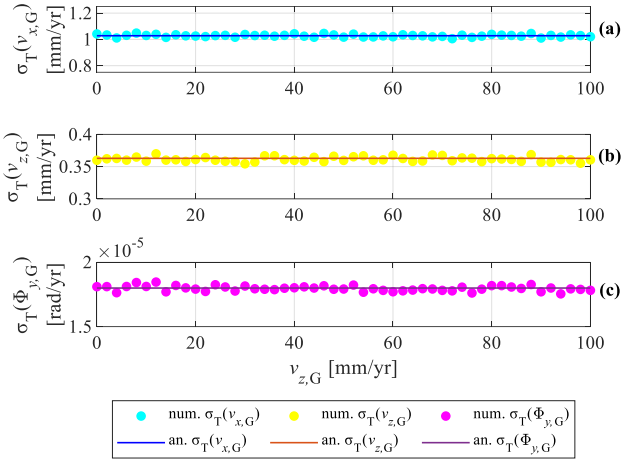

Figure 19. Influence of $v_{z,G}$ on the total uncertainties: σ_T of $v_{x,G}$ (a), $v_{z,G}$ (b) and $\Phi_{y,G}$ (c).

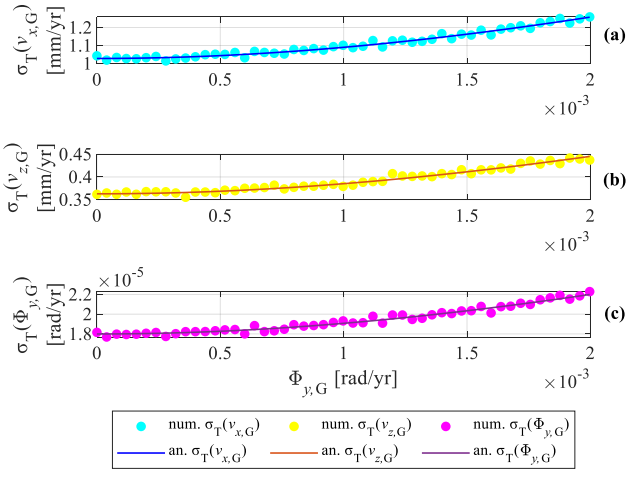

Figure 20. Influence of $\Phi_{y,G}$ on the total uncertainties: σ_T of $v_{x,G}$ (a), $v_{z,G}$ (b) and $\Phi_{y,G}$ (c).

DOI: 10.3217/978-3-99161-057-1-121

Rigid motion of wind turbines can be generally associated with foundation settlement, a gradual phenomenon that can potentially cause damage to both structural and non-structural elements. Traditional Structural Health Monitoring techniques typically require extended acquisition times, making them economically impractical, particularly in foundation settlement cases. In contrast, satellite-based monitoring allows for the direct analysis of historical displacement time series without the need for on-site instrumentation, while enabling the monitoring of displacements over large areas with high accuracy. The proposed approach utilizes the mean annual displacement of permanent scatterers along the lines of sight, thereby eliminating the need for temporal and spatial resampling of satellite data.

The accuracy of the proposed approach was evaluated using Monte Carlo numerical simulations, in which satellite data were generated while accounting for uncertainties in both the displacement of the considered scatterers (measurement errors) and their vertical positioning along the wind turbine (positioning errors). The numerical results were then compared with those derived from the analytical expressions initially presented in [14] and adapted for application to wind turbines. The satellite data parameters were based on those of the COSMO-SkyMed constellation, which is particularly well-suited for structural monitoring applications. Numerical errors and analytical uncertainties were evaluated across various scenarios, including variations in the 3D motion components and the number of available PSs on the turbine. As expected, an increased number of available PSs leads to reduced uncertainties, while larger turbine rotations result in greater errors. In contrast, the uncertainties remain uncorrelated with both vertical and horizontal translations.

The method presents certain limitations, including the approximation of the turbine as a purely rigid body, which necessitates fitting the data to a rigid model without accounting for possible structural deformations. Additionally, the approach relies on Permanent Scatterers (PS), which – depending on the processing technique – can be affected by noise due to both decorrelation and atmospheric effects, potentially impacting the accuracy of the results. Nevertheless, the strong agreement observed between numerical simulations and analytical predictions confirms the robustness of the proposed procedure in estimating the rigid-body motion of wind turbines and the associated uncertainties. The method demonstrates high precision, with uncertainties on the order of tenths of millimeters and/or milliradians per year.

The next steps of the research involve attempting to obtain a priori estimates of the uncertainty based solely on the knowledge of the potential number of PS present, to assess whether satellite data can already provide the required accuracy during the phase of selecting the monitoring methodology. For this purpose, simplifications regarding the distribution of PS will be made. Additionally, data from a wind farm will be analyzed to evaluate the possibility of applying the methodology to real cases.

ACKNOWLEDGMENTS

This study was carried out within the ReLUIS-DPC 2024–2026 Project (Line WP6). The financial support of the Civil Protection Department of the Presidency of the Council of Ministers and the Reluis Consortium is gratefully acknowledged.

REFERENCES

[1] Global Wind Energy Council, Global Wind Report 2023, 2023. Available at: https://www.gwec.net/.

[2] M. Martinez-Luengo, A. Kolios and L. Wang, Structural health monitoring of offshore wind turbines: A review through the Statistical Pattern Recognition Paradigm, *Renewable and Sustainable Energy Reviews* 64: 91-105, 2016.

[3] W. Liu, B. Tang and Y. Jiang, Status and problems of wind turbine structural health monitoring techniques in China, *Renewable Energy*, 35: 1414-1418, 2010.

[4] M. Currie, M. Saafi, C. Tachtatzis and F. Quail, Structural integrity monitoring of onshore wind turbine concrete foundations, *Renewable Energy* 83: 1131-1138, 2015.

[5] S. K. Gupta, D. P. Shukla and K. C. Niraj, Kortupi landslide deformation study in non-urban area using DInSAR and MTInSAR techniques on Sentinel-1 SAR data, *Advances in Space Research*, 70(12): 3878-3891, 2022.

[6] M. Crosetto, L. Solari, M. Mróz, J. Balasis-Levinsen, N. Casagli, M. Frei, A. Oyen, D. A. Moldestad, L. Bateson, L. Guerrieri, V. Comerci and H. S. Andersen, The evolution of wide-area DInSAR: From regional and national services to the European ground motion service, *Remote Sensing*, 12(12), 2020.

[7] A. Miano, A. Mele, D. Calacaterra, D. D. Martire, D. Infante, A. Prota e M. Ramondini, The use of satellite data to support the structural health monitoring in areas affected by slow-moving landslides: a potential application to reinforced concrete buildings, *Structural Health Monitoring*, 20(6): 3265-3287, 2021.

[8] D. Talledo, A. Stella, M. Bonano, F. Di Carlo, R. Lanari, M. Manunta, A. Meda, A. Mele, A. Miano, A. Prota e A. Saetta, Techniques for Structural Assessment Based on MT-DInSAR Data, Applied to the San Michele Complex in Rome, *European Workshop on Structural Health Monitoring. EWSHM 2022*, pp. 593-603, 2023.

[9] A. Ferretti, C. Prati and F. Rocca, Permanent Scatterers in SAR Interferometry, *IEEE Transactions on Geoscience and Remote Sensing*, 39(1), 2001.

[10] F. Mancini, F. Grassi and C. Nicola, A workflow based on snap–stamps open-source tools and gnss data for psi-based ground deformation using dual-orbit sentinel-1 data: Accuracy assessment with error propagation analysis, *Remote Sensing*, 13(753): 1-23, 2021.

[11] M. Crosetto, O. Monserrat, R. Iglesias and B. Crippa, Persistent Scatterer Interferometry: Potential, Limits and Initial C- and X-band Comparison, *Photogrammetric Engineering & Remote Sensing*, 76(9): 1061-1069, 2010.

[12] D. A. Talledo, A. Miano, M. Bonano, F. Di Carlo, R. Lanari, M. Manunta, A. Meda, A. Mele, A. Prota, A. Saetta e A. Stella, Satellite radar interferometry: Potential and limitations for structural assessment and monitoring, *Journal of Building Engineering*, 46: 103756, 2022.

[13] F. Di Carlo, A. Miano, I. Giannetti, A. Mele, M. Bonano, R. Lanari, A. Meda e A. Prota, On the integration of multi-temporal synthetic aperture radar interferometry products and historical surveys data for buildings structural monitoring, *Journal of Civil Structural Health Monitoring*, 11(5,): 1429-1447, 2021.

[14] E. Bassoli, L. Vincenzi, F. Grassi and F. Mancini, A multi-temporal DInSAR-based method for the assessment of the 3D rigid motion of buildings and corresponding uncertainties, *Journal of Building Engineering*, 73: 106738, 2023.

[15] A. Ferretti, G. Savio, R. Barzaghi, A. Borghi, S. Musazzi, F. Novali, C. Prati and F. Rocca, Submillimeter accuracy of InSAR time series: Experimental validation, *IEEE Transactions on Geoscience and Remote Sensing*, 45: 1142-1153, 2007.

[16] S. Gernhardt and R. Bamler, Deformation monitoring of single buildings using meter-resolution SAR data in PSI, *ISPRS Journal of Photogrammetry and Remote Sensing*, 73: 68-79, 2012.

[17] B. Zhang, L. Chang and A. Stein, Spatio-temporal linking of multiple SAR satellite data from medium and high resolution radarsat-2 images, *ISPRS Journal of Photogrammetry and Remote Sensing*, 176: 222-236, 2021.

[18] J. A. Barros and A. Mathern, Recent and future trends of onshore wind turbine foundations, in *IABSE Symposium Prague 2022*, Prague, Czech Republic, 2022.